A major purpose of the Technical Information Center is to provide the broadest dissemination possible of information contained in DOE's Research and Development Reports to business, industry, the academic community, and federal, state and local governments.

Although a small portion of this report is not reproducible, it is being made available to expedite the availability of information on the research discussed herein.

LA-UR -85-3621

Los Alamos National Laboratory is operated by the University of California for the United States Department of Energy under contract W-7405-ENG-36

TITLE HMS-BURN: A MODEL FOR HYDROGEN DISTRIBUTION AND COMBUSTION IN NUCLEAR REACTOR CONTAINMENTS

LA-UR--85-3621

TI86 002418

AUTHOR(S): John R. Travis

SUBMITTED TO Thirteenth Water Reactor Safety Research Information Meeting
Gaithersburg, Maryland
October 22-25, 1985

DISCLAIMER

Los Alamos Los Alamos National Laboratory
Los Alamos, New Mexico 87545

HMS-BURN: A MODEL FOR HYDROGEN DISTRIBUTION AND COMBUSTION IN NUCLEAR REACTOR CONTAINMENTS

J. R. Travis, Los Alamos National Laboratory
Theoretical Division, Group T-3, MS-B216
Los Alamos, New Mexico 87545
505-667-9089

ABSTRACT

It is now possible to analyze the time-dependent, fully three-dimensional behavior of hydrogen combustion in nuclear reactor containments. This analysis involves coupling the full Navier-Stokes equations with multi-species transport to the global chemical kinetics of hydrogen combustion. A transport equation for the subgrid scale turbulent kinetic energy density is solved to produce the time and space dependent turbulent transport coefficients. The heat transfer coefficient governing the exchange of heat between fluid computational cells adjacent to wall cells is calculated by a modified Reynolds analogy formulation. The analysis of a MARK-III containment indicates very complex flow patterns that greatly influence fluid and wall temperatures and heat fluxes.

NOMENCLATURE

A_w	Wall Area
A_α	Coefficient of specific heat
B_α	Coefficient of specific heat
C_D	Structural drag coefficient
C_p	Specific heat at constant pressure
C_v	Specific heat at constant volume
$\bar{D}$	Structural drag vector
$\bar{g}$	Gravitational vector
h_s	Structure heat transfer coefficient
h_w	Wall heat transfer coefficient
H_2	Hydrogen
H_2O	Water vapor
I	Specific internal energy and radial index
I_o	Specific internal energy at reference temperature
J	Axial index
K	Azimuthal index
L	Length scale
M	Molecular weight
N_2	Nitrogen
O_2	Oxygen
p	Pressure
Q	Energy source or sink
Q_c	Energy of combustion
Q_r	Radiated energy due to combustion
Q_s	Energy exchange with internal structure
Q_t	Decay of turbulent energy into thermal energy
Q_{tc}	Total chemical energy of combustion
Q_w	Convected energy exchanged with walls
q	Turbulent kinetic energy
q_r	Radiated energy to wall surface
q_w	Convected energy to wall surface
q_{wr}	Radiated energy from wall surface
r	Radial Dimension
R_α	Gas constant
S	Mass source or sink
t	Time
T	Temperature
u	Radial velocity
$\bar{u}$	Velocity vector
v	Axial velocity
w	Azimuthal velocity
X_α	Mass fraction
z	Axial dimension
β	Wall thermal diffusivity
γ	Apparent or total diffusivity
δr	Computational cell size in radial dimension
δt	Time step
$\delta\theta$	Computational cell size in azimuthal dimension
δz	Computational cell size in axial dimension
ε	Emissivity
κ	Apparent or total conductivity
λ	Second coefficient of apparent or total viscosity
μ	First coefficient of apparent or total viscosity
ν	Apparent or total kinematic viscosity
ρ	Density
σ	Stefan-Boltzmann constant
$\bar{\tau}$	Viscous stress tensor
θ	Azimuthal dimension
$\dot{\omega}$	Reaction rate

Subscripts

b	Boundary
c	Chemical energy
i	Radial index
j	Axial index
k	Azimuthal index
o	Reference
r	Radiated energy
ref	Reference
s	Structure
w	Wall
α	Specie

I. INTRODUCTION

It has recently become of interest to analyze hydrogen diffusion flames above the pool in the wet-well of the MARK-III containment. In this accident sequence, a transient event from 100% power, the reactor is scrammed but there is a loss of all coolant-injection capability. The reactor vessel remains pressurized as the coolant water in the reactor vessel begins to boil away. When the core becomes uncovered and heats up, after roughly 40 minutes into the accident, zirconium and steel oxidation leads to the generation of hydrogen which is then released through safety relief valves (SRV's) into the suppression pool. Under certain conditions, this release of hydrogen (e.g., with an ignition source) leads to the formation of diffusion flames above the release areas in the suppression pool. These flames may persist in localized regions above the suppression pool for tens of minutes and therefore could lead to overheating of nearby penetrations in the dry-well or wet-well walls. It is of most interest to calculate the temperature and pressure of the containment atmosphere in the wet-well region and the temperatures and heat flux loads on the dry-well and wet-well walls up to 10 m above the suppression pool surface where key equipment and penetrations are located. Another major contribution of this analysis is the calculation of the induced flow patterns which allows identification of oxygen starved regions and regions where diffusion flames may lift off the suppression pool surface. In order to simulate this problem, we have extended the capabilities of the Hydrogen Mixing Studies code (HMS)[1-3] to include combustion, a generalized subgrid scale turbulence model, and a comprehensive wall heat transfer treatment.

II. MATHEMATICAL MODEL

The partial-differential equations that govern the fluid dynamics, species transport and turbulence model and the equations modeling the hydrogen combustion and heat transfer processes are presented in this section.

A. The Mixture Equations

The mixture mass conservation equation is

$$\frac{\partial \rho}{\partial t} + \nabla\cdot(\rho\bar{u}) = 0 \quad , \tag{1}$$

where

$\rho = \sum_{\alpha=1}^{4} \rho_\alpha$; ρ_α = macroscopic density of the individual species (H_2O, N_2, H_2 or O_2),

$\bar{u}$ = mass-average velocity vector.

The mixture-momentum conservation equations are given by

$$\frac{\partial(\rho\bar{u})}{\partial t} + \nabla\cdot(\rho\bar{u}\bar{u}) = -\nabla p + \nabla\cdot\bar{\tau} + \hat{\rho}\bar{g} - \bar{D} \quad , \tag{2}$$

where

p = pressure,

$\bar{\tau}$ = viscous stress tensor,

$\hat{\rho}$ = local density relative to the average density

$\bar{g}$ = gravitational vector, and

$\bar{D}$ = structural drag vector.

The viscous force, $\nabla\cdot\bar{\tau}$, is the ususal Newtonian one, where, for example, the radial component is given by

$$\frac{1}{r}\frac{\partial}{\partial r}(r\tau_{rr}) + \frac{1}{r}\frac{\partial \tau_{r\theta}}{\partial \theta} - \frac{\tau_{\theta\theta}}{r} + \frac{\partial \tau_{rz}}{\partial z} \tag{3}$$

where

$$\tau_{rr} = \mu\left[2\frac{\partial u}{\partial r} - \frac{2}{3}\nabla\cdot\bar{u}\right] \quad , \tag{4}$$

$$\tau_{r\theta} = \mu\left[r\frac{\partial}{\partial r}\left(\frac{v}{r}\right) + \frac{1}{r}\frac{\partial u}{\partial \theta}\right] \quad , \tag{5}$$

$$\tau_{\theta\theta} = \mu\left[2\left(\frac{1}{r}\frac{\partial v}{\partial \theta} + \frac{u}{r}\right) - \frac{2}{3}\nabla\cdot\bar{u}\right] \quad , \tag{6}$$

and

$$\tau_{rz} = \mu\left[\frac{\partial v}{\partial r} + \frac{\partial u}{\partial z}\right] \quad . \tag{7}$$

The coefficient of viscosity, μ, which appears in the viscous stress tensor, is interpreted as an "apparent" or "total" viscosity. Here we have assumed the second viscosity coefficient $\lambda = -2\mu/3$, which is equivalent to assuming the bulk

viscosity to be zero. The calculation of the apparent viscosity through the turbulence model will be discussed below. The structural drag vector is given by $\bar{D} = C_D \rho (\text{Area/Volume}) \bar{u}|\bar{u}|$, where Area/Volume = (structure area)/(structure volume), and $C_D = 1$.

The mixture internal energy density equation is

$$\frac{\partial(\rho I)}{\partial t} + \nabla\cdot(\rho I\bar{u}) = -p\nabla\cdot\bar{u} + \nabla\cdot(\kappa\nabla T) + Q_c + Q_t - Q_s - Q_w + Q \qquad (8)$$

where

- I = mixture specific internal energy,
- κ = apparent or total conductivity,
- T = mixture temperature,
- Q_c = energy source per unit volume and time due to the chemical energy of combustion,
- Q_t = energy source per unit volume and time due to the decay of turbulent into thermal energy,
- Q_s = energy per unit volume and time exchanged with the internal structure,
- Q_w = energy per unit volume and time exchanged with the walls, and
- Q = energy source per unit volume and time, for example, the energy reradiated from the walls.

B. Constitutive Relationships

The specific internal energy is related to the temperature by

$$I = \sum_{\alpha=1}^{4} X_\alpha (I_o)_\alpha + \sum_{\alpha=1}^{4} X_\alpha \int_{T_o}^{T} (C_v)_\alpha \, dT \quad ,$$

where X_α is the mass fraction, $(I_o)_\alpha$ is the specific internal energy at the reference temperature, T_o, for specie α and the specific heats at constant volume, $(C_v)_\alpha$, have been represented over the temperature range (200, 2500) degrees Kelvin by the linear approximation $(C_v)_\alpha = A_\alpha + B_\alpha T$.

The equation-of-state for the average fluid pressure P_o is given by the ideal gas mixture equation

$$P_o = T \sum_{\alpha=1}^{4} R_\alpha \rho_\alpha \quad , \qquad (10)$$

where R_α is the gas constant for specie α. The apparent conductivity is found by assuming the Prandtl Number, Pr, equal to unity, i.e., $\text{Pr} = C_p\mu/\kappa = 1$, thus $\kappa = C_p\mu$, where

$$C_p = \sum_{\alpha=1}^{4} X_\alpha (C_p)_\alpha = \sum_{\alpha=1}^{4} X_\alpha [R_\alpha + (C_v)_\alpha] \quad . \qquad (11)$$

C. Heat Transfer Relationships

The energy source/sink terms are now examined in detail. The energy source term due to combustion, Q_c, is given as a fraction of the total chemical energy of combustion, Q_{tc}, which is described by the Arrenhius chemical kinetics reaction rate, $\dot{\omega}$, in

$$2H_2 + O_2 \overset{\dot{\omega}}{\Leftrightarrow} 2H_2O + Q_{tc} \quad . \qquad (12)$$

We discuss this further in the chemical kinetics section, however, for the purpose of this analysis we assume[4]

$$Q_c = 0.85 Q_{tc} \quad , \qquad (13)$$

with the partitioning of the remaining 15% to energy radiated from a point source at the computational cell center to the walls using the appropriate view factors. For the sake of completeness, we define

$$Q_r = 0.15 Q_{tc} \quad . \qquad (14)$$

The term representing the decay of turbulent energy into thermal energy, Q_t, is discussed in detail in the turbulence model section.

The heat exchange between the gas and the internal structure, Q_s, is given by

$$Q_s = q_s/V \quad , \qquad (15)$$

where

$$q_s = m_s C_{vs} \frac{dT_s}{dt} = h_s A_s (T - T_s) \quad . \qquad (16)$$

In these expressions

- V = computational cell volume,
- m_s = mass of internal structure in a computational cell,
- T_s = structure temperature,

h_s = heat transfer coefficient between the gas and the structure, and
A_s = area of exposed structure in a computational cell.

By writing the right hand side of the differential Eq. (16) at the advanced time level, the advanced time level T_s^{n+1} can be found as

$$T_s^{n+1} = \frac{m_s C_{vs} T_s^n + h_s A_s T^{n+1} \delta t}{m_s C_{vs} + h_s A_s \delta t} \quad . \tag{17}$$

It is straightforward to obtain an implicit relationship for the heat exchange between the gas and structure that is valid for all values for the heat transfer coefficient, h_s, as

$$q_s = \frac{h_s A_s m_s C_{vs}}{m_s C_v + h_s A_s \delta t} \left(T^{n+1} - T_s^n\right) \quad . \tag{18}$$

The heat flux between a fluid computational cell adjacent to a wall or floor is given by

$$Q_w = q_w / V \quad , \tag{19}$$

where

$$q_w = h_w A_w (T - T_w) \quad . \tag{20}$$

The thermal boundary layer is accounted for by using a modified Reynolds analogy formulation[5] and simplifying to derive the heat transfer coefficient

$$h_w = (\tau_w / u_c) C_p \quad . \tag{21}$$

We define A_w as the area of wall or floor exposed to a fluid cell, T_w as the wall surface temperature, T as the fluid temperature at the position of the cell centered average velocity u_c, and τ_w as the wall shear stress, which is related to the fluid density and the wall shear speed by $\tau_w = \rho u_*^2$. We are not able to resolve turbulent boundary layers near solid walls with any practical computing mesh, so we elect to match our solution near solid boundaries with the turbulent law-of-the-wall[6]

$$\frac{u_c}{u_*} = A \ln \left(\frac{y u_*}{\nu}\right) + B \quad . \tag{22}$$

This expression requires an iterative solution for u_*. We find that it is more convenient and almost as accurate to use the approach of CONCHAS-SPRAY[7] and use an approximation obtained by replacing u_* in the argument of the logarithm in Eq. (22) by the one-seventh power law.[8] This expression may be rearranged to give

$$\frac{y u_*}{\nu} = 0.15 \left(\frac{y u_c}{\nu}\right)^{7/8} \quad , \tag{23}$$

which yields

$$\frac{u_c}{u_*} = .19 \ln \left(\frac{y u_c}{\nu}\right) + 0.76 \tag{24}$$

when substituted into Eq. (22) with A = 2.5 and B = 5.5. Now it is straightforward to find the shear speed u_*, where y is the distance from the wall to the cell centered average velocity u_c and ν is the molecular kinematic viscosity.

The Reynolds number $y u_c / \nu$ may be small, thus indicating the point in question lies in the laminar sublayer and the law-of-the-wall formulation is not valid. In this case, Eq. (24) is replaced by the corresponding laminar formula

$$\frac{u_c}{u_*} = (y u_c / \nu)^{1/2} \quad . \tag{25}$$

The transition between Eqs. (24) and (25) is made at the value where they predict the same u_*, which is $y u_c / \nu = 130.7$. Therefore, u_* is calculated by Eq. (24) when $y u_c / \nu \geq 130.7$, and by Eq. (25) when $y u_c / \nu < 130.7$. In the laminar case, the wall heat transfer coefficient Eq. (21) reduces to $h_w = \rho \nu / y$, which results, when substituted into Eq. (20), in a simple difference approximation to the laminar heat flux for a molecular Prandtl number of unity.

The wall shear stress is also applied as a velocity boundary condition. For example, the expression Eq. (3) when evaluated for fluid cells adjacent to a horizontal solid boundary requires Eq. (7) to be computed on the boundary surface. This leads to the finite-difference representation of $\frac{\partial u}{\partial z}$ on the boundary while preserving $\tau_{rz} = \tau_w$. In other words, the boundary condition velocity for the radial component on a horizontal surface is

$$u_b = u_{i+1/2,j,k} - \delta z \cdot \tau_w / \mu \quad , \tag{26}$$

where $u_{i+1/2,j,k}$ is the cell faced radial velocity component adjacent to a horizontal solid boundary. Note that when $\mu >> \delta z \cdot \tau_w$, the boundary condition velocity is very nearly the adjacent fluid velocity, which indicates a near free-slip velocity boundary condition.

For every computational cell side interfacing with area A_w to a wall or floor, the one-dimensional transient heat conduction equation

$$\frac{\partial T}{\partial t} = \beta \frac{\partial^2 T}{\partial x^2} \quad , \tag{27}$$

with the wall boundary condition

$$\sum q_r + q_w - q_{wr} = - kA_w \frac{\partial T_w}{\partial x} \tag{28}$$

is solved for the wall temperature distribution, T, and the wall surface temperature, T_w. The sum total of radiant energy from combustion falling on A_w is given by $\sum q_r$, q_w is calculated from Eq. (20), and q_{wr} is the energy radiated away from the surface defined by

$$q_{wr} = A_w \sigma (\varepsilon_w T_w^4 - T_{ref}^4) \quad . \tag{29}$$

In order to simplify the radiation heat transfer treatment, we define T_{ref} equal to the wall temperature directly across the wet-well from the wall segment we are radiating from. This reradiated energy from the walls, q_{wr}, is summed over all reradiating surfaces, $\sum_s (q_{wr})_s$, and then added uniformly to all computational cells in the wet-well as

$$Q = \sum_s (q_{wr})_s / V_T \quad , \tag{30}$$

where V_T is the total volume of all computational cells in the wet-well that have Q added as a source term.

D. The Species Transport Equations

The dynamics of the individual species are determined by

$$\frac{\partial \rho_{H_2O}}{\partial t} + \nabla \cdot (\rho_{H_2O} \bar{u}) - \nabla \cdot \left[\rho \gamma \nabla \frac{\rho_{H_2O}}{\rho} \right] = S_{H_2} + S_{O_2} \tag{31}$$

$$\frac{\partial \rho_{N_2}}{\partial t} + \nabla \cdot (\rho_{N_2} \bar{u}) - \nabla \cdot \left[\rho \gamma \nabla \frac{\rho_{N_2}}{\rho} \right] = 0 \quad , \tag{32}$$

$$\frac{\partial \rho_{H_2}}{\partial t} + \nabla \cdot (\rho_{H_2} \bar{u}) - \nabla \cdot \left[\rho \gamma \nabla \frac{\rho_{H_2}}{\rho} \right] = -S_{H_2} \quad , \tag{33}$$

and

$$\frac{\partial \rho_{O_2}}{\partial t} + \nabla \cdot (\rho_{O_2} \bar{u}) - \nabla \cdot \left[\rho \gamma \nabla \frac{\rho_{O_2}}{\rho} \right] = -S_{O_2} \quad , \tag{34}$$

where the apparent or total diffusivity, γ, is determined by setting the Schmidt Number to unity, $\gamma = \mu/\rho$ and S_{H_2} and S_{O_2} are determined by the chemical kinetics presented below. Summing the above species transport equations results in the mixture mass conservation equation.

E. Turbulence Model

The turbulence model is a subgrid scale transport model that was developed for the KIVA computer code.[9,10] This model is formulated in terms of the turbulent kinetic energy per unit mass, q, which represents turbulent length scales too small to resolve in the mesh, and the local fluid density, ρ. The transport equation for the product ρq is given by

$$\frac{\partial}{\partial t}(\rho q) + \nabla \cdot (\rho q \bar{u}) = - \frac{2}{3} \rho q \nabla \cdot \bar{u} + \bar{\tau} : \nabla \bar{u} + \nabla \cdot (\mu \nabla q) - \rho q^{3/2} / L \quad , \tag{35}$$

where the second term on the left hand side represents the convection of turbulence by the established velocity field while the terms on the right hand side respectively represent the effects of turbulence generation by compression, production of turbulence by viscous dissipation, diffusion of turbulence, and decay of turbulent energy into thermal energy. This last term appears with opposite sign as a source term in the thermal internal energy density Eq. (8), so

$$Q_t = \rho q^{3/2} / L \quad , \tag{36}$$

where L is a characteristic length on the order of twice the computational cell size. Actually, for this calculation, we set L equal to the diagonal of the three-dimensional computational cell. The apparent or total viscosity, μ, is given by the sum of the turbulent and molecular values, where the turbulent viscosity, μ_t, is computed by

$$\mu_t = \rho L q^{1/2}/20 \quad , \tag{37}$$

so

$$\mu = \mu_t + \mu_m \quad . \tag{38}$$

By assuming the Prandtl and Schmidt numbers to equal unity, we can define respectively the apparent or total conductivity and diffusivity as

$$\kappa = \mu C_p \quad , \tag{39}$$

and

$$\gamma = \mu/\rho \quad . \tag{40}$$

It is interesting to note that in the quasi-steady solution where the production term due to viscous dissipation equals the decay term, this generalized model reduces to the original algebraic subgrid scale model of the type used by Smagorinsky[11] and Deardorff.[12,13]

F. Chemical Kinetics

We are employing global chemical kinetics in which the only reaction modeled is

$2H_2 + O_2 \overset{\dot{\omega}}{\rightarrow} 2H_2O + Q_{tc}$, which is similar to the chemical kinetics models in other Los Alamos combustion codes.[7,9,10,14-16] Hydrogen combustion proceeds by means of many more elementary reaction steps and intermediate chemical species. The chemical reaction time scale is, however, very short compared with fluid dynamic motions and meaningful calculations can be accomplished using this simplified global chemical kinetics scheme.[17] Here, Q_{tc} is the chemical energy of combustion per unit volume and time, i.e.,

$$Q_{tc}\left(\frac{W}{m^3}\right) = 4.778 \times 10^5 \left(\frac{J}{mole}\right)\dot{\omega}\left(\frac{mole}{m^3 \cdot s}\right) .$$

The reaction rate, $\dot{\omega}$, is modeled by Arrenhius kinetics as

$$\dot{\omega} = C_f \left(\frac{\rho}{M}\right)_{H_2} \left(\frac{\rho}{M}\right)_{O_2} \exp(-10^4/T) \quad , \tag{41}$$

where M is the molecular weight and

$C_f = 3.3 \times 10^5 \left(\frac{m^3}{mole - s}\right)$. Now, the source terms S_H and S_{O_2} are found by $S_{H_2} = 2M_{H_2}\dot{\omega}$, and $S_{O_2} = M_{O_2}\dot{\omega}$.

III. SOLUTION PROCEDURE

The above equations are written in finite-difference form for their numerical solution. The nonlinear finite-difference equations are then solved iteratively using a point relaxation method. Since we are interested in low-speed flows where the propagation of pressure waves need not be resolved, we are therefore utilizing a modified ICE[18] solution technique where the species densities are functions of the containment pressure, and not of the local pressure. Time-dependent solutions can be obtained in one-, two-, and three-space dimensions in plane and in cylindrical geometries, and in one- and two-space dimensions in spherical geometries. The geometric region of interest is divided into many finite-sized space-fixed zones called computational cells that collectively form the computing mesh. Figure 1 shows a typical computational cell with the velocities centered on cell boundaries. All scalar quantities, such as I, p, T, q, and ρ_α's are positioned at the cell-center designated (i,j,k). The finite-difference equations for the quantities at time $t=(n+1)\delta t$ form a system of coupled, nonlinear algebraic equations.

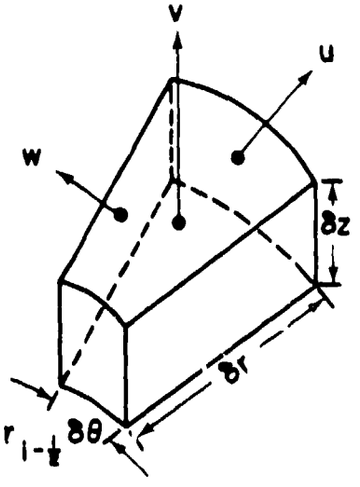

Fig. 1. Locations of velocity components for a typical cell in cylindrical geometry.

The solution method starts with the explicit calculation of the chemical kinetics yielding the source terms in the species transport equations, specific internal energy density equation, and the radiated energy from the combustion process. Next, the convection, turbulent

stress-tensor, gravity, and drag terms are evaluated in the mixture momentum equations, and an estimate of the time advanced velocities is obtained. The solution method then proceeds with the iteration phase in which the densities, pressure, and velocities are calculated to simultaneously satisfy the mass equations, momentum equations, and the equation of state. After the iteration phase is complete, the specific internal energy density equation with all the heat transfer processes are computed, and the turbulent transport equation is evaluated to calculate the turbulent transport coefficients. The computational time step is then finished with the advancement of the time step. The reader is referred to references 1-3 for more details on the solution procedure.

IV. GEOMETRY, COMPUTATIONAL MESH, AND INITIAL AND BOUNDARY CONDITIONS

The MARK-III containment design is shown schematically in Fig. 2. We are only concerned with the containment volume above the water level so we approximate the containment with a right circular cylinder (37.8 m diameter and 51.2 m high) configuration which has the same atmospheric containment volume as that of Fig. 2. The outer vertical containment wall (wet-well wall) is concrete 0.75 m (2.5 feet) thick and the inner vertical wall (dry-well wall) is concrete 1.5 m (5 feet) thick. The annular region between these two walls is called the wet-well. Hydrogen spargers or sources are actually at the bottom of the suppression pool as indicated in Fig. 2 and are within 3 m of the inner wall. The nine sources can be thought of as circular, 3 m diameter, centered azimuthally at 16, 48, 88, 136, 152, 184, 256, 288, and 328 degrees. Fig. 3 gives the idea of the sources relative to the wet-well and the containment walls.

The geometry as shown in the two simplified perspective views of Figs. 4 and 5 indicates the true three-dimensionality of the containment with the concrete floors, penetrations, and enclosed volumes. The hydrogen sources are shown at the bottom as small rectangular regions. The cylindrical computational mesh approximating this geometry is presented in Fig. 6 which shows each of the computing zones. A pie-shaped region of the computing mesh indicating the dimensions is presented in Fig. 7. Hydrogen enters the computing mesh at the bottom (J=2) of specific cells in the annular ring (I=8) with a temperature equaling 71°C and pressure equaling 10^5 Pa. The azimuthal positions of the hydrogen sources within the ring I=8 are specified at K = 4, 6, 8, 13, 15, 16, 20, 22, and 24 which corresponds to computational zones centered at 322.5, 292.5, 262.5, 187.5, 157.5, 142.5, 82.5, 52.5, and 22.5, respectively. A mass flow rate of 45.5 kg/min is for 30 minutes distributed equally among the nine sources. The initial condition in the containment is dry air at 21°C and 10^5 Pa.

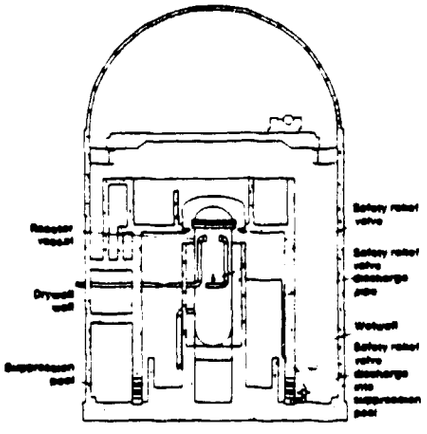

Fig. 2. Schematic view of the MARK-III containment design showing the suppression pool, wet-well, and safety relief valve discharge position.

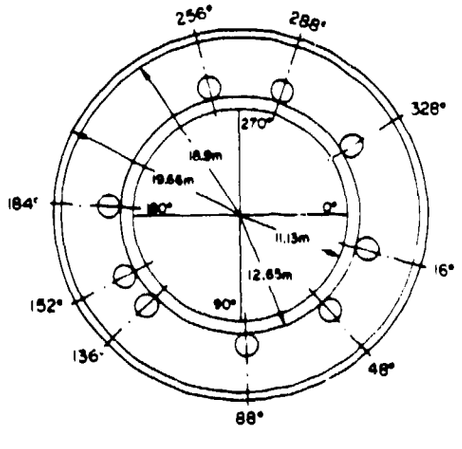

Fig. 3. Schematic view of the MARK-III containment design showing the nine hydrogen spargers (sources) relative to the wet-well.

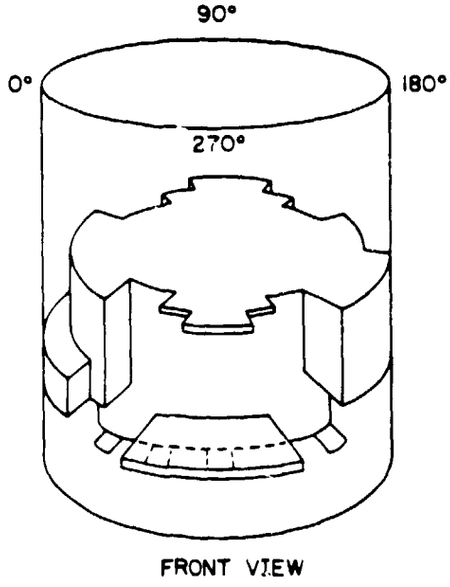

Fig. 4. Perspective front view of containment showing excluded volumes, concrete floors, and locations of hydrogen sources.

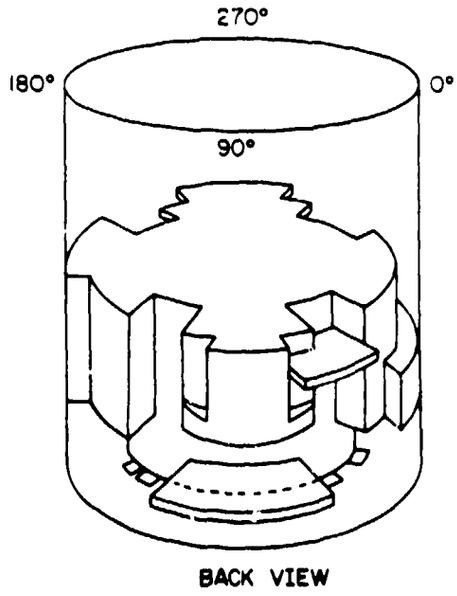

Fig. 5. Perspective back view of containment showing excluded volumes, concrete floors, and locations of hydrogen sources.

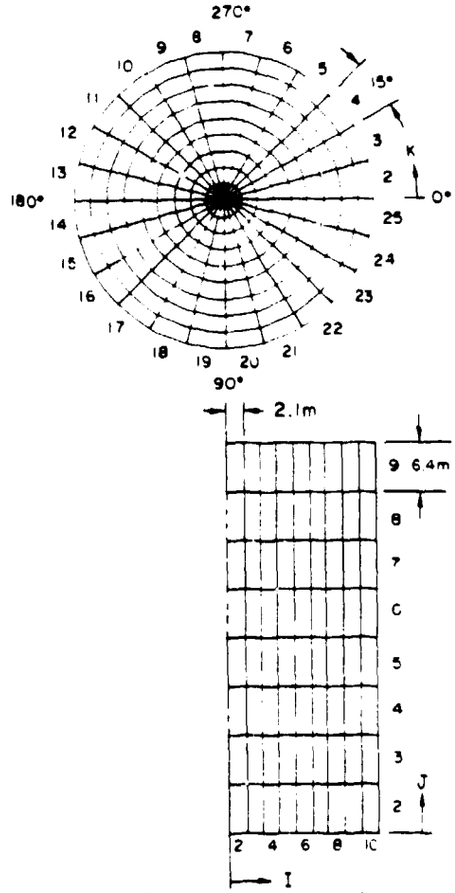

Fig. 6. Computing mesh for containment geometry.

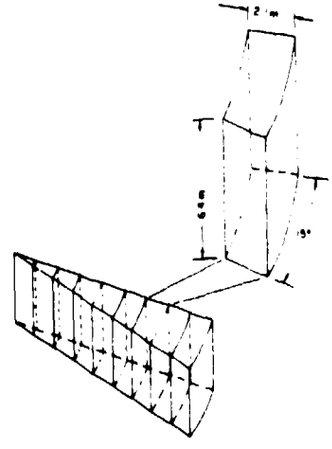

Fig. 7. Perspective view of a pie-shaped zone within the computing mesh.

There are tremendous heat sinks in the containment, e.g., 2.2 x 10^6 kg steel with heat transfer surface area equalling 2.7 x 10^4 m^2, from which an average surface area per unit volume for four axial zones can be found. The structural heat transfer and drag formulations both use this average value to compute heat and momentum exchange, respectively, within a computational zone.

V. RESULTS

Figures 8-10 display velocity vectors in an unwrapped (constant radius vs height) configuration at 900 s for radial locations 13.65 m, 15.75 m, and 17.85 m, respectively. These three radial cells cover the wet-well region. For Fig. 8, the radius is at the radial center of the hydrogen source cells (I=8), which can be seen at the bottom of the plot by the flow openings. For example, there is a double source between 135 and 165 degrees and seven single sources distributed along the azimuthal dimension. With nine distributed sources, and distributed as they are, the Figures show the development of very strong buoyancy driven flows in the partial hot chimney at 45 degrees and the full hot chimneys at 135 and 315 degrees. A cold chimney (downflow) develops at 225 degrees completing the convective loops, althougn at the outer wall, Fig. 10 indicates several convective cells where downflow is observed, e.g., 22.5, 127.5, 172.5, and 337.5 degrees. The outer wall tends to be much cooler, which allows fluid to cool and sink in these zones. The partial hot chimney (45 degrees) is blocked by a concrete

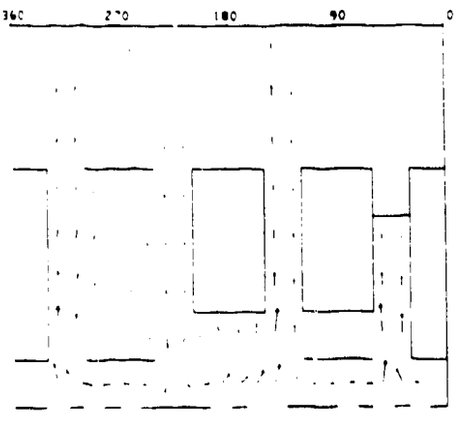

Fig. 8. Unwrapped (axial dimension, z vs constant radius, I=9 or 13.65 m) velocity vectors at 900 s. V_{max} = 4.4 m/s and W_{max} = 2.6 m/s.

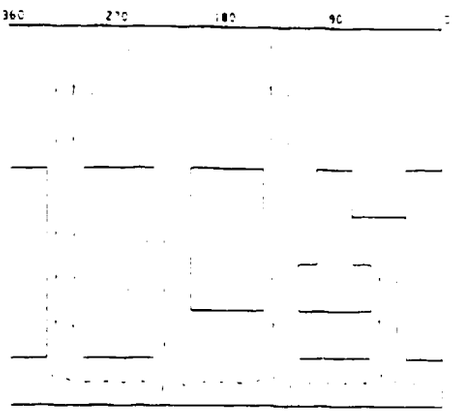

Fig. 9. Unwrapped (axial dimension, z vs constant radius, I=9 or 15.75 m) velocity vectors at 900 s. V_{max} = 2.3 m/s and W_{max} = 1.9 m/s.

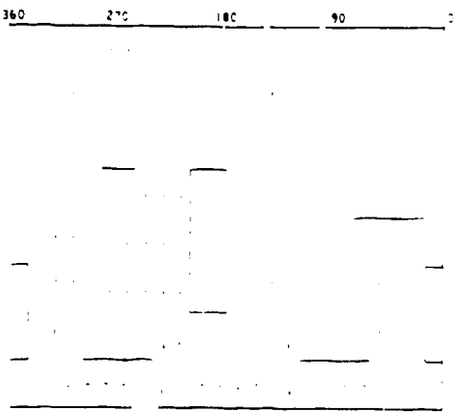

Fig. 10. Unwrapped (axial dimension, z vs constant radius, I=10 or 17.85 m) velocity vectors at 900 s. V_{max} = 1.8 m/s and W_{max} = 1.5 m/s.

floor about half way to the top. The flow is diverted toward the outer wall and then either upward around the floor or contributing to the convective cells at 0 and 90 degrees. These convective cells are seen in Fig. 10 to be around the enclosed volume at 0 degrees and above the lowest floor at 90 degrees respectively. The horizontal lines designate concrete floors where no mass, momentum or energy is allowed to flux across. Thus we see the hot products of combustion beneath the floor at say 270 degrees convecting horizontally and contributing to the full hot chimney at 315 degrees.

Gas temperature at radius 13.65 m, inner wall temperature and inner wall heat flux contours at 900 s are shown in Figs. 11-13, respectively. As one would expect maximum values are generally found in regions of hydrogen sources. Note that the contour plotting routine does not recognize the concrete floors which are thin compared to the cell height. The resolution under the floors is insufficient to actually show any contours; however, the idea of high/low concentrations and gradients is clearly demonstrated.

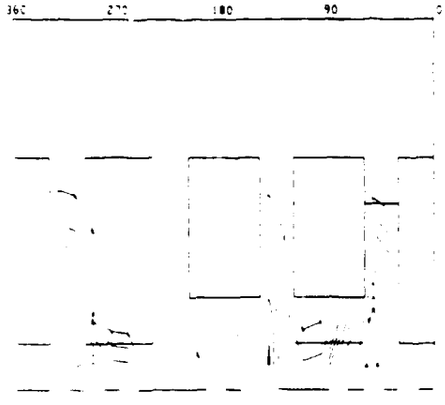

Fig. 11. Unwrapped (axial dimension, z vs constant radius, I=6 or 13.65 m) gas temperature contours at 900 s.
T_H = 1145 K, T_L = 390 K, and
ΔT_W = 94.2 K.

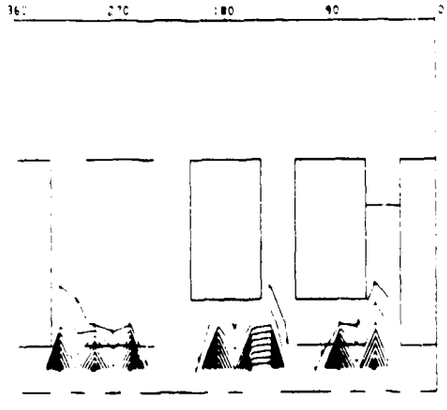

Fig. 12. Unwrapped (axial dimension, z vs constant radius, r=12.6 m) inner wall temperature contours at 900 s.
T_{W_H} = 671 K, T_{W_L} = 335 K, and
ΔT_W = 41.9 K.

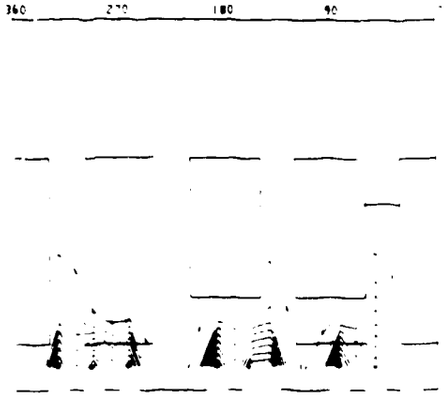

Fig. 13. Unwrapped (axial dimension, z vs constant radius, r=12.6 m) inner wall heat flux contours at 900 s.
Q_{W_H} = 10.3 kW/m^2, Q_{W_L} = 1.1 kW/m^2, and
ΔQ_W = 1.14 kW/m^2.

A horizontal cut through the containment at 3.2 m above the suppression pool surface (Figs. 14 and 15) depicts respectively the gas temperature and wall heat flux contours at 900 s. Maximum temperatures occur at 22.5 and 52.5 degrees. Sources in this region are far removed from the strong cold chimney at 225 degrees and therefore do not benefit from the intense convection mixing of cool gas into the combustion process, which tends to keep flame temperatures much cooler. Note that Fig. 11 was unable to show the hot gas above the source at 22.5 degrees and below the enclosed volume. This is because insufficient spatial resolution exists here to draw the contours. Figures 16-19 give gas temperatures at radius 15.75 m, gas temperatures at radius 17.85 m, outer wall temperatures, and outer wall heat fluxes, all at 900 s, respectively. The gas temperatures clearly show the convection and diffusion of heat from the hydrogen combustion region. Note that the temperature and heat flux on the outer wall (Figs. 18 and 19) are much more uniform than the inner wall (Figs. 12 and 13). This is largely due to the fact that the outer wall is exposed to a more uniform radiation heating than is the inner wall.

Summary results are presented in the next figures. Figure 20 shows the maximum and minimum wet-well temperatures and containment atmosphere pressure. Note that the maximum temperature would always be the adiabatic flame temperature for the composition of gases at that particular time. We correctly calculate the adiabatic flame temperature; however, because of the

coarseness of the computational mesh, the average temperature of any zone in which combustion is taking place will always be lower than the actual adiabatic flame temperature. Mass histories for H_2O, H_2, and O_2 are also included in Fig. 20.

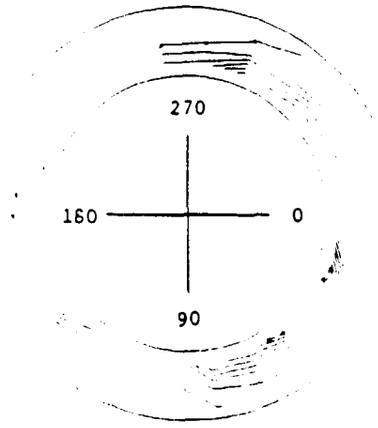

Fig. 14. Gas temperature contours, 3.2 m (J=2) above the pool surface at 900 s. T_H = 1145 K, T_L = 400 K, and ΔT = 93.2 K.

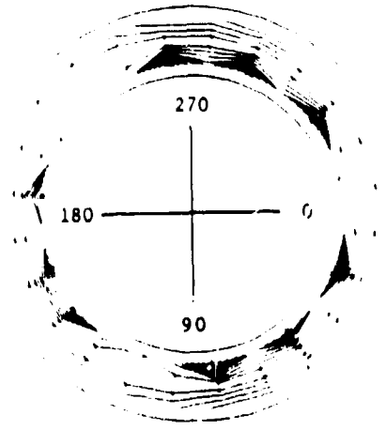

Fig. 15. Wall heat flux contours 3.2 m (J=2) above the pool surface at 900 s. Q_{W_H} = 10.3 KW/m^2, Q_{W_L} = 1.1 KW/m^2, and ΔQ_W = 1.14 KW/m^2.

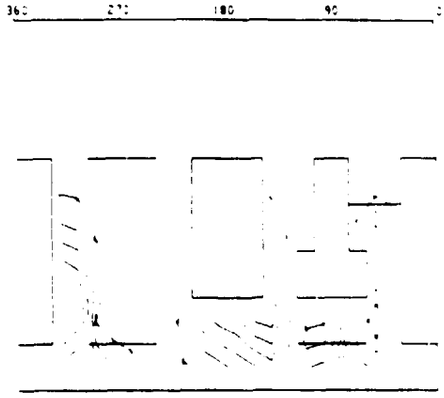

Fig. 16. Unwrapped (axial dimension, z vs constant radius, I=9 or 15.75 m) gas temperature contours at 900 s. T_H = 770 K, T_L = 349 K, and ΔT = 52.6 K.

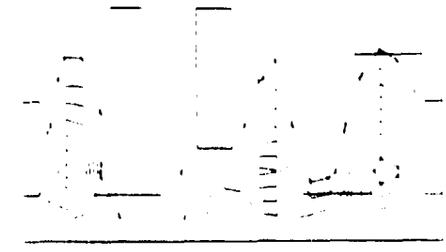

Fig. 17. Unwrapped (axial dimension, z vs constant radius, I=10 or 17.85 m) gas temperature contours at 900 s. T_H = 651 K, T_L = 335 K, and ΔT = 39.5 K.

Note at roughly 1200 s significant amounts of hydrogen begins to accumulate in the containment. This indicates that there are regions that are becoming starved for oxygen[2] as the oxygen is depleted, and the hydrogen moves higher above the suppression pool before burning. At the same time, there is an increase in the slope of the pressure-time curve due to hydrogen combusting higher in the containment where there is less internal structure absorbing the energy of combustion, so more energy remains in the gas. The containment pressure is however well within the design criteria.

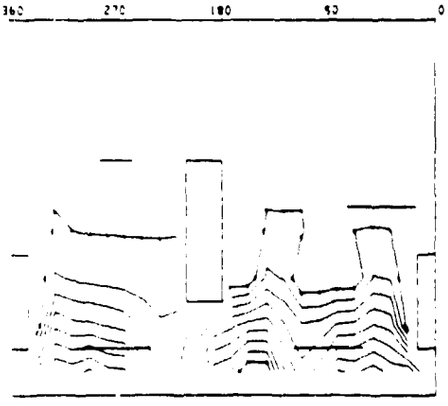

Fig. 18. Unwrapped (axial dimension, z vs constant radius, r=18.9 m) outer wall temperature contours at 900 s. T_{W_H} = 439 K, T_{W_L} = 302, and ΔT_W = 17.1 K.

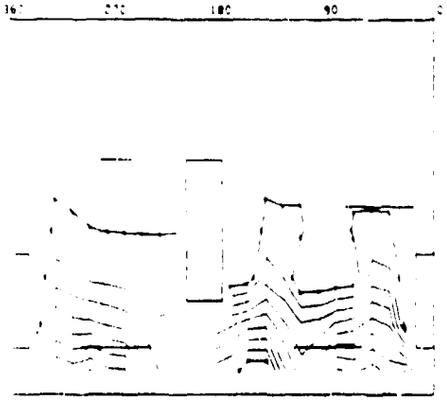

Fig. 19. Unwrapped (axial dimension, z vs constant radius, r=18.9 m) outer wall heat flux contours at 900 s. Q_{W_H} = 5.8 KW/m^2, Q_{W_L} =314 W/m^2, and ΔQ = 684 W/m^2.

Spatial wall temperature and heat flux distributions on the inner (wet-well) and outer (dry-well) walls at 3.3 m (10 feet) and 10 m (30 feet) above the pool surface are presented in Figs. 21-22 for various times (30, 90, 270, 810, and 1620 seconds). The hydrogen sparger or source azimuthal positions are indicated on each

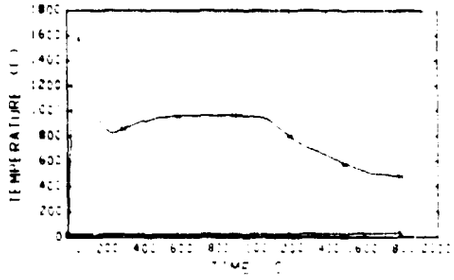

Fig. 20a. Maximum and minimum atmospheric wet-well temperatures.

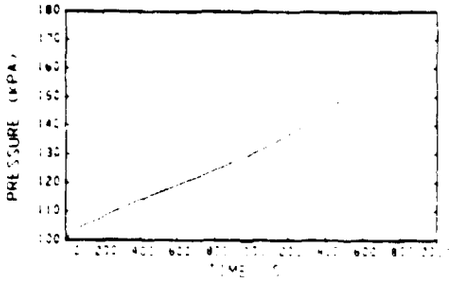

Fig. 20b. Containment pressure.

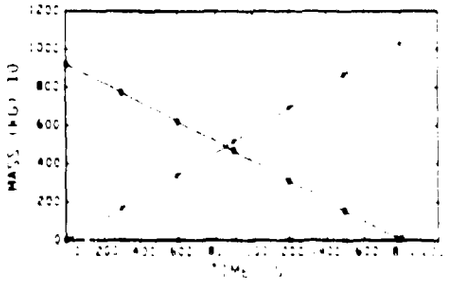

Fig. 20c. Mass of O_2, H_2O, and H_2 in containment.

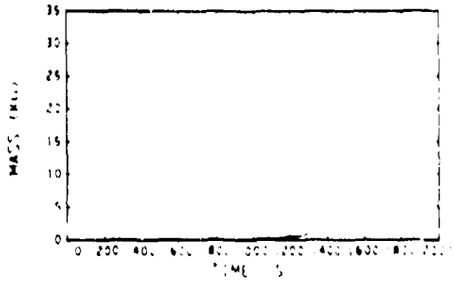

Fig. 20d. Mass of H_2 in containment.

figure. Maximum heat flux values are seen to correspond one for one to the sparger locations. For azimuthal location 142.5 degrees, one of the locations where large values of heat fluxes and temperature occur, we present in Figs. 23 and 24 inner and outer wall temperature and heat flux histories at 3.3 m and 10 m above the pool surface. The heat flux at 3.3 m on the inner wall peaks early and then decreases as heat is convected to other regions of the containment. At the 10 m level, the heat flux is fairly constant as the velocity field develops and becomes somewhat steady. There is a sudden decrease in the 3.3 m level heat flux at approximately 1425 s, with a corresponding increase at the 10 m level. This indicates the flame elongating and lifting up into the containment for a short period before both curves show the decrease as oxygen is depleted in this region. Wall temperatures on the other hand show steady increasing values until oxygen is depleted and then decreasing values. Reradiated energy at the 3.3 m heat flux level on the inner surface becomes important at about 500 s when the wall temperature surpasses 300 C. This is evidenced by the decrease in the temperature slope as the temperature begins to approach an asymtotic value of about 500 C. Most of the heat transferred to the outer wall is radiated to these surfaces from the burning hydrogen. These heat fluxes are more or less constant until just before oxygen depletion when the 10 m curve increases. Temperatures on the outer wall almost constantly increase in time but are rather low in value, only reaching 260 C at the 3.3 m level.

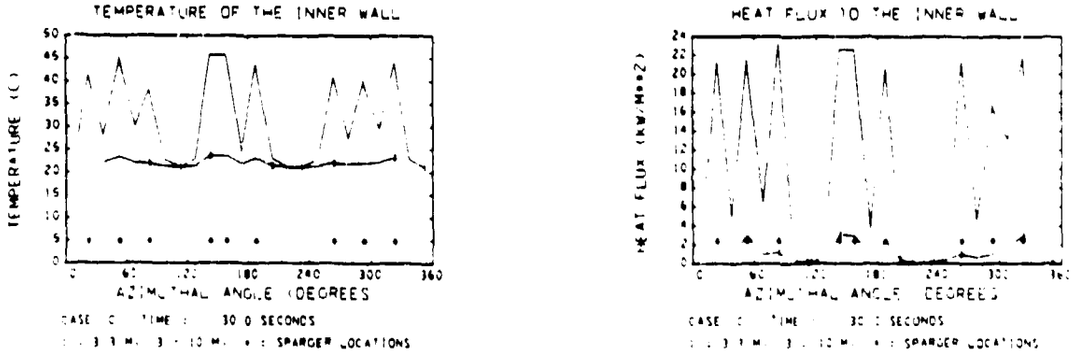

Fig. 21a. Inner wall temperature and heat flux at 30 s.

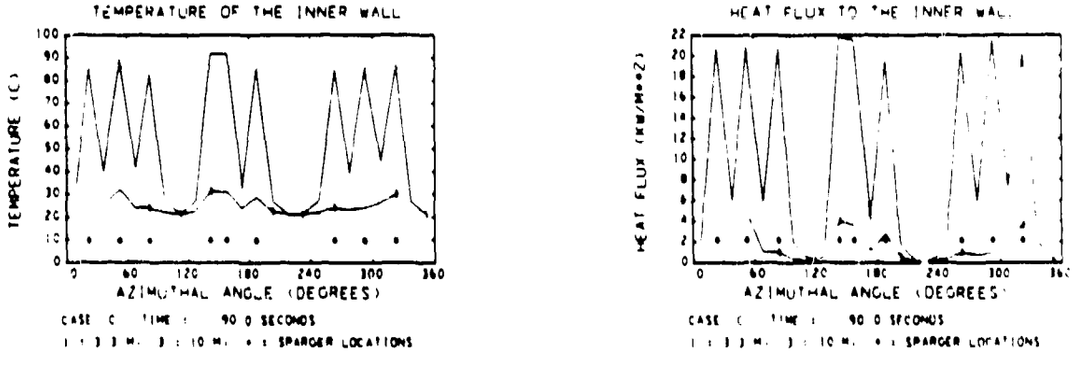

Fig. 21b. Inner wall temperature and heat flux at 90 s.

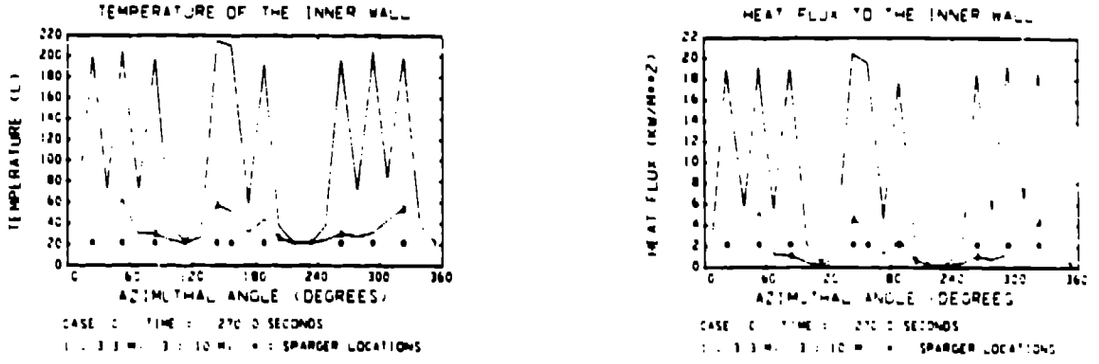

Fig. 21c. Inner wall temperature and heat flux at 270 s.

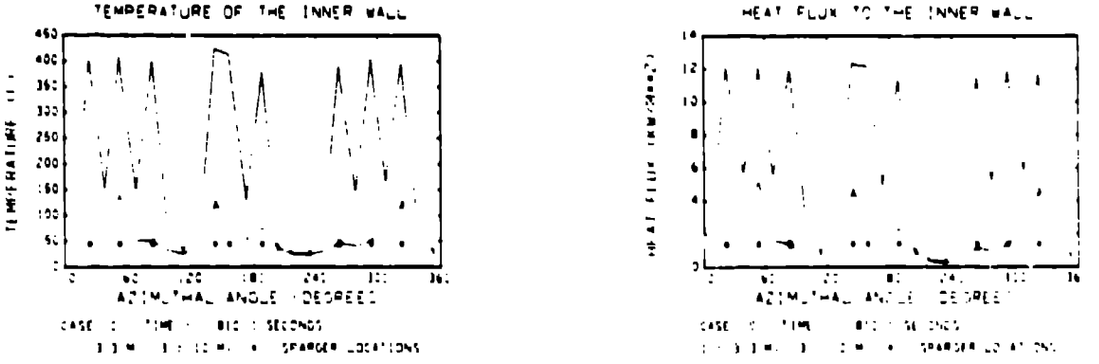

Fig. 21d. Inner wall temperature and heat flux at 810 s.

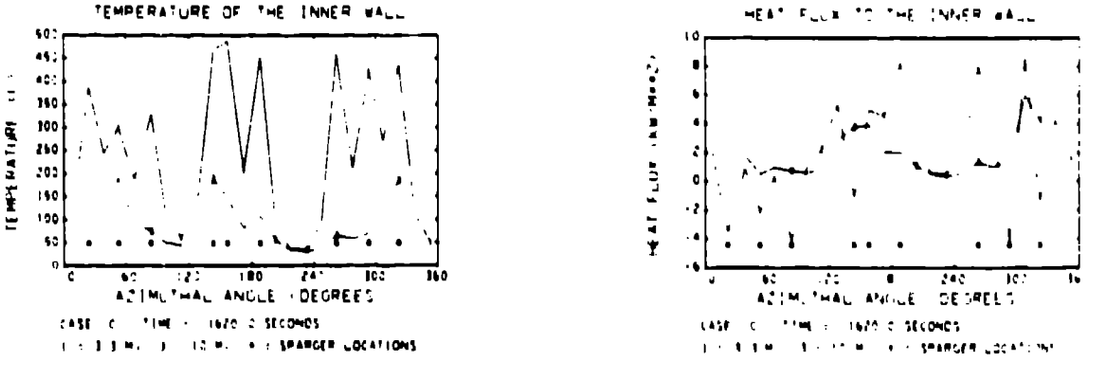

Fig. 21e. Inner wall temperature and heat flux at 1620 s.

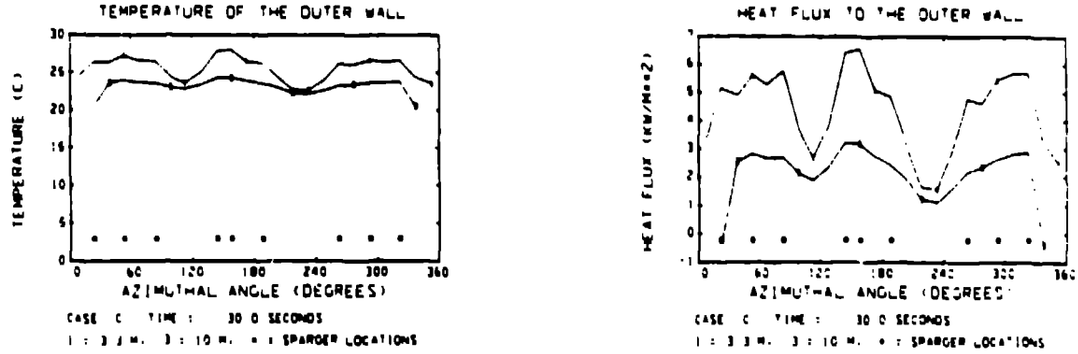

Fig. 22a. Outer wall temperature and heat flux at 30 s.

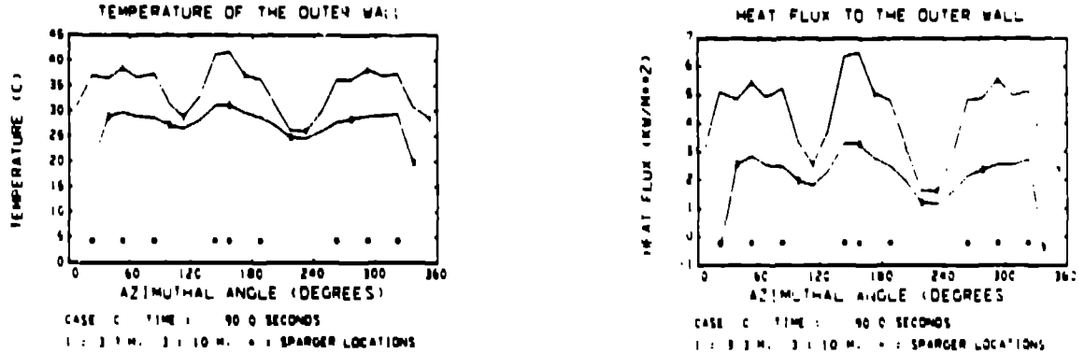

Fig. 22b. Outer wall temperature and heat flux at 90 s.

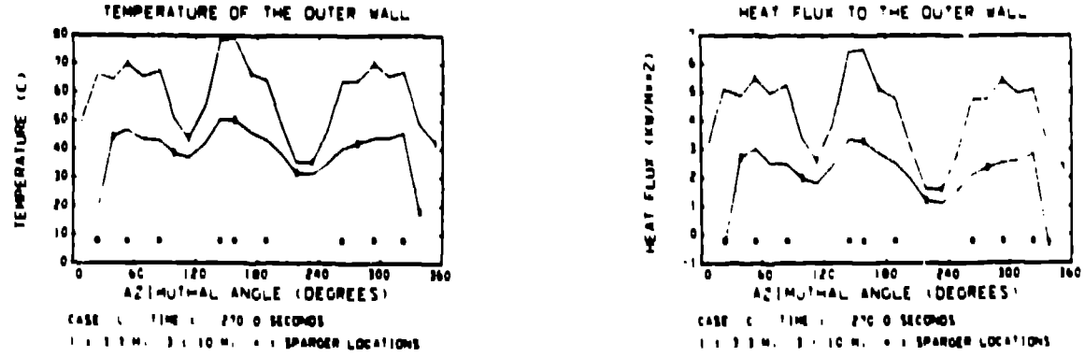

Fig. 22c. Outer wall temperature and heat flux at 270 s.

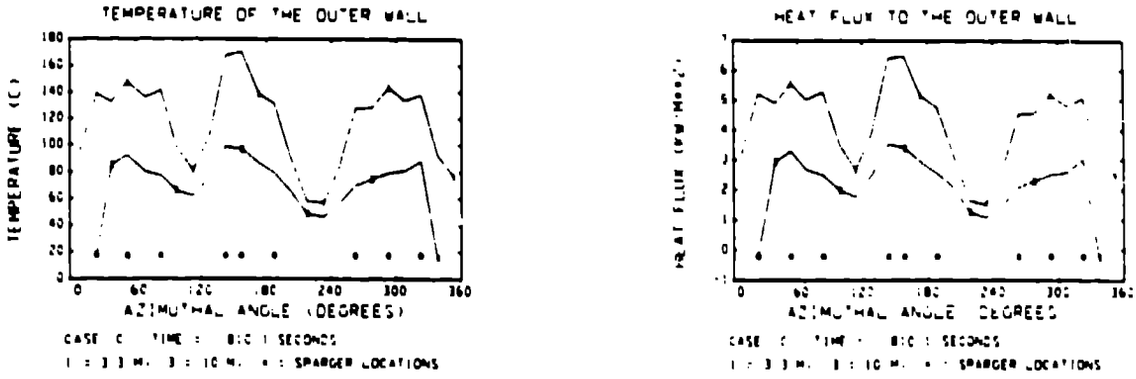

Fig. 22d. Outer wall temperature and heat flux at 810 s.

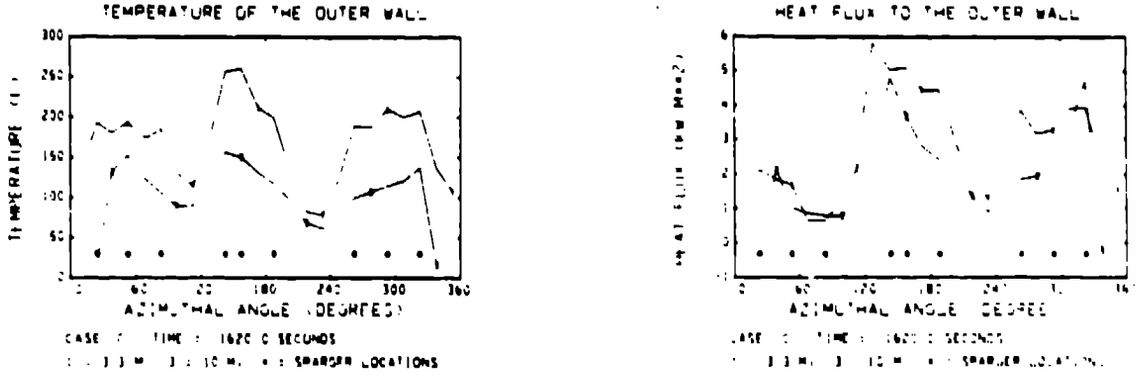

Fig. 22e. Outer wall temperature and heat flux at 1620 s.

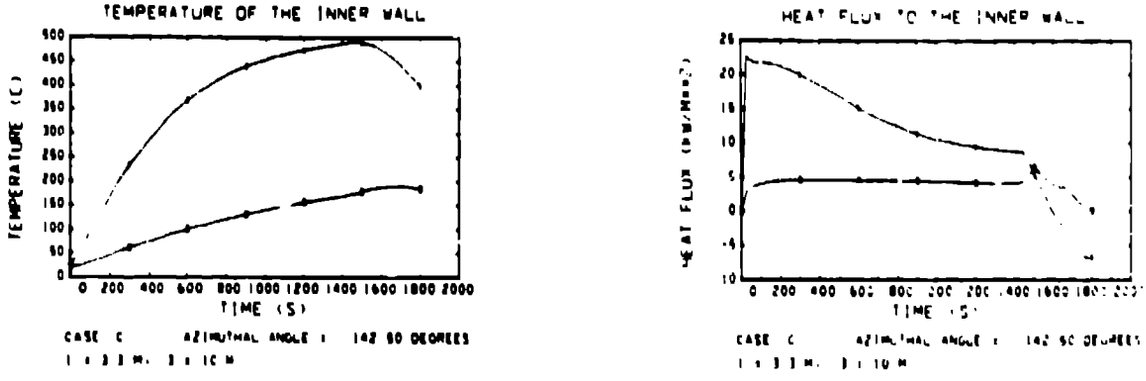

Fig. 23. Temperature and heat flux histories on the inner wall at 142.5 azimuthal degrees.

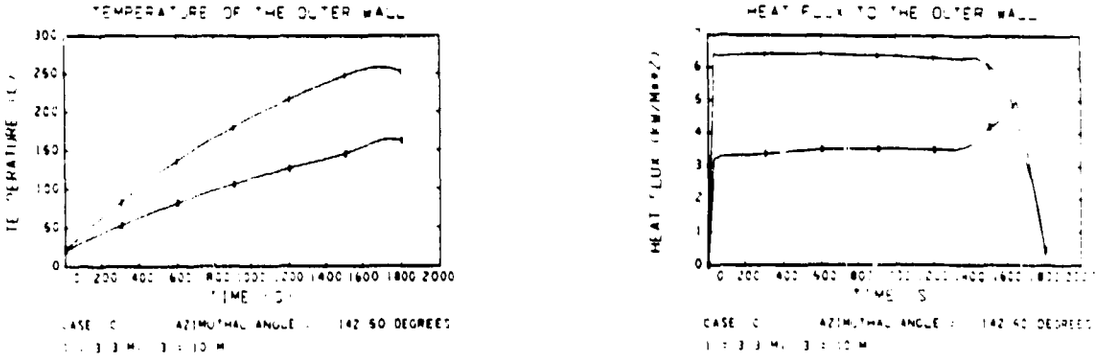

Fig. 24. Temperature and heat flux histories on the outer wall at 142.5 azimuthal degrees.

Without a flame model or resolving flame details with a finely zoned computational mesh, it is impossible for us to supply details about the flame such as flame height, flame width and flame angle. We can say, however, that most of the combustion takes place in the inlet cell (flame height 6 m), as long as there is sufficient oxygen for combustion. Once flames become oxygen starved, then it is possible for flames to lift off the water surface and burn higher in the wet-well, perhaps even reattaching to the water surface if more oxygen is supplied by convection.

VI. CONCLUSIONS

Differences between the present analysis, which incorporates a generalized subgrid scale turbulence model, law-of-the-wall heat transfer coefficient calculation, and comprehensive wall temperature distribution calculation, and the identical transient analyzed and reported in Ref. 2 exist primarily in the wall heat flux loads. In the present analysis, there is a general decrease and more uniform heat flux load to the inner wall by roughly 40% and approximately a 50% increase to the outer wall during the early part of the transient when these loads are maximum. Later in the transient there are smaller differences. It should be noted that early in time the heat flux loads on the outer wall are only about one-quarter those on the inner wall at the 3.3 m level and about equal at the 10 m level. It is apparent that the improved turbulence model which indicates enhanced mixing, and the calculation of a time and space dependent heat transfer coefficient (rather than the constant value used in Ref. 2) are responsible for the decreased heat flux loads.

In strictly conserving mass, momentum, and energy throughout the computational mesh, this time-dependent, fully three-dimensional calculation is the most detailed analysis to date for diffusion flames in reactor containments. Improvements can be made in the turbulence model, convective heat transfer treatment, radiation heat transfer modeling, and the chemical kinetics representation; however, the effects of these phenomena are accounted for, and the fluid dynamics of the overall induced flow patterns are relatively insensitive to changes in these parameters.

VII. ACKNOWLEDGMENTS

It is a pleasure to express appreciation to J. D. Ramshaw for his helpful discussions relating to the turbulence model. This work was performed under the auspices of the United States Nuclear Regulatory Commission.

VIII. REFERENCES

1. J. R. Travis, "HMS: A Model for Hydrogen Migration Studies in LWR Containments," Second Intern. Workshop on the Impact of Hydrogen on Water Reactor Safety, October 3-7, 1982, Albuquerque, NM.

2. J. R. Travis, "Hydrogen Diffusion Flames in a MARK III Containment," Joint ANS/ASME Conference on Design, Construction, and Operation of Nuclear Power Plants, August 5-8, 1984, Portland, OR.

3. J. R. Travis, "HMS: A Computer Program for Transient, 3-D Mixing Gases," Los Alamos National Laboratory report LA-10267-MS, NUREG/CR-4020 (1985).

4. Bob Zalosh, Factory Mutual Corporation, Norwood, MA, personal communication (1984).

5. B. E. Launder and D. B. Spalding, "The Numerical Computation of Turbulent Flows," Comp. Maths. Appl. Mech. Eng. 3, 269 (1974).

6. H. Schlichting, Boundary-Layer Theory, 6th ed. (McGraw-Hill, New York, 1968).

7. L. D. Cloutman, J. K. Dukowicz, J. D. Ramshaw, and A. A. Amsden, "CONCHAS-SPRAY: A Computer Code for Reactive Flows with Fuel Sprays," Los Alamos National Laboratory report LA-9294-MS (May 1982).

8. R. S. Brodkey, The Phenomena of Fluid Motions (Addison Wesley, Reading, MA, 1969).

9. A. A. Amsden, J. D. Ramshaw, P. J. O'Rourke, and J. K. Dukowicz, "KIVA: A Computer Program for Two- and Three-Dimensional Fluid Flows with Chemical Reactions and Fuel Sprays," Los Alamos National Laboratory report LA-10245-MS (1985).

10. A. A. Amsden, T. D. Butler, P. J. O'Rourke, and J. D. Ramshaw, "KIVA: A Comprehensive Model for 2D and 3D Engine Simulations," SAE Intern. Congress and Exhibition, February 27-March 2, 1985, Detroit, MI.

11. J. Smagorinsky, "General Circulation Experiments with the Primitive Equations," Monthly Weather Rev. 91, 99 (1963).

12. J. W. Deardorff, "A Numerical Study of Three-Dimensional Turbulent Channel Flow at Large Reynolds Numbers," J. Fluid Mech. 41, 453 (1970).

13. J. W. Deardorff, "On the Magnitude of the Subgrid Scale Eddy Coefficient," J. Comput. Phys. 7, 120 (1971).

14. W. C. Rivard, O. A. Farmer, and T. D. Butler, "RICE: A Computer Program for Multicomponent Chemically Reactive Flows at All Speeds," Los Alamos Scientific Laboratory report LA-5812 (March 1975).

15. J. D. Ramshaw and J. K. Dukowicz, "APACHE: A Generalized-Mesh Eulerian Computer Code for Multicomponent Chemically Reactive Fluid Flow," Los Alamos Scientific Laboratory report LA-7427 (January 1979).

16. T. D. Butler, L. D. Cloutman, J. K. Dukowicz, and J. D. Ramshaw, "CONCHAS: An Arbitrary Lagrangian-Eulerian Computer Coded for Multicomponent Chemically Reactive Fluid Flow at All Speeds," Los Alamos Scientific Laboratory report LA-8129-MS (November 1979).

17. T. D. Butler, L. D. Cloutman, J. K. Dukowicz, and J. D. Ramshaw, "Multi-dimensional Numerical Simulation of Reactive Flow in Internal Combustion Engines," Prog. Energy Combust. Sci. 7, 293 (1981).

18. F. H. Harlow and A. A. Amsden, "Numerical Fluid Dynamics Calculation Method for All Flow Speeds," J. Comput. Phys. 8, 197 (1971).